Carr, M.; Meakins, A.; Silburn, S. A.; Karhunen, J.; Bernert, M.; Bowman, C.; Callarelli, A.;
Carvalho, P.; Giroud, C.; Harrison, J. R.; Henderson, S. S.; Huber, A.; Lipschultz, B.; Lunt, T.;
Moulton, D.; Reimold, F.

Physically principled reflection models applied to filtered camera imaging inversions in metal walled fusion machines

M. Carr (iD), A. Meakins, S. A. Silburn, J. Karhunen, M. Bernert, C. Bowman, A. Callarelli (iD), P. Carvalho, C. Giroud, J. R. Harrison, S. S. Henderson (iD), A. Huber, B. Lipschultz (iD), T. Lunt, D. Moulton, F. Reimold, ASDEX Upgrade Team, JET Contributors, MAST-Upgrade Team, and EUROfusion MST1 Team

View Online   **Export Citation**   **CrossMark**

Physically principled reflection models applied to filtered camera imaging inversions in metal walled fusion machines

View Online   Export Citation   CrossMark

M. Carr,[1,a] A. Meakins,[1] S. A. Silburn,[1] J. Karhunen,[2] M. Bernert,[3] C. Bowman,[4] A. Callarelli,[1] P. Carvalho,[1] C. Giroud,[1] J. R. Harrison,[1] S. S. Henderson,[1] A. Huber,[5] B. Lipschultz,[4] T. Lunt,[3] D. Moulton,[1] F. Reimold,[6] ASDEX Upgrade Team,[b] JET Contributors,[c] MAST-Upgrade Team,[d] and EUROfusion MST1 Team[e]

AFFILIATIONS

[1] UKAEA/CCFE, Culham Science Centre, Abingdon, Oxon OX14 3DB, United Kingdom

[2] Department of Applied Physics, Aalto University School of Science, P.O. Box 11100, FI-00076 Aalto, Finland

[3] Max-Planck-Institut für Plasmaphysik, 85748 Garching, Germany

[4] Department of Physics, York Plasma Institute, University of York, Heslington, York, United Kingdom

[5] Forschungszentrum Jülich GmbH, Institut für Energie-und Klimaforschung - Plasmaphysik, 52425 Jülich, Germany

[6] Max-Planck-Institut für Plasmaphysik, Greifswald, Germany

[a] matthew.carr@ukaea.uk
[b] See the authors list in A. Kallenbach *et al.*, "Overview of ASDEX Upgrade results," Nucl. Fusion **57**, 102015 (2017).
[c] See the authors list in X. Litaudon *et al.*, "Overview of the JET results in support to ITER," Nucl. Fusion **57**, 102001 (2017).
[d] See the authors list in A. Kirk *et al.*, "Overview of recent physics results from MAST," Nucl. Fusion **57**, 102007 (2017).
[e] See the authors list in H. Meyer *et al.*, "Overview of progress in European medium sized tokamaks towards an integrated plasma-edge/wall solution," Nucl. Fusion **57**, 102014 (2017).

ABSTRACT

Ray-tracing techniques are applied to filtered divertor imaging, a diagnostic that has long suffered from artifacts due to the polluting effect of reflected light in metal walled fusion machines. Physically realistic surface reflections were modeled using a Cook-Torrance micro-facet bi-directional reflection distribution function applied to a high resolution mesh of the vessel geometry. In the absence of gonioreflectometer measurements, a technique was developed to fit the free parameters of the Cook-Torrance model against images of the JET in-vessel light sources. By coupling this model with high fidelity plasma fluid simulations, photo-realistic renderings of a number of tokamak plasma emission scenarios were generated. Finally, a sensitivity matrix describing the optical coupling of a JET divertor camera and the emission profile of the plasma was obtained, including full reflection effects. These matrices are used to perform inversions on measured data and shown to reduce the level of artifacts in inverted emission profiles.

https://doi.org/10.1063/1.5092781

I. INTRODUCTION

Accurate diagnosis of plasma characteristics in the divertor is crucial for our understanding of detachment physics, plasma-surface interactions and ensuring the technical success of the ITER and DEMO devices. Filtered camera imaging is a useful technique for filling the diagnostic gap that exists between the plasma core and the scrape-off layer (SOL).

The core plasmas of tokamaks are well diagnosed, for example, bulk plasma parameters can be measured with good spatial resolution from diagnostics such as Thomson scattering and charge exchange recombination spectroscopy.[1] Many of the core plasma quantities are to a good approximation flux functions; hence, measurement of 1D spatial profiles is often sufficient. In the SOL, however, plasma parameters are no longer flux functions and become

(at least) 2D. Langmuir probes embedded in the plasma facing components provide good measurements at the plasma-material interface and other regions with measurable plasma interaction. However, there is a diagnostic gap between these two regions where it is difficult to achieve spatially resolved measurements of the plasma species' temperatures and densities. Line ratio analysis of line integrated spectroscopy can yield localized measurements[2] but fails to provide the spatial resolution we have come to expect from core diagnostics.

Filtered cameras can give the required spatial resolution and have been deployed with some success in carbon walled machines.[3] However, utilizing these for routine physics analysis in metal walled machines has proven more challenging due to reflection effects.[4–6] The reflected light of bright plasma regions, such as the strike-points or x-point, by wall features can lead to artifacts in the measured images. Sometimes it is difficult to discern which features in the image are due to direct plasma emission and which are artifacts. It often prohibits routine/automated analysis of such images. Mitigating techniques such as optical dumps or wall blackening cannot be used because of the wide field of view and the need for wall protection. Reflection effects are, therefore, one of the main impediments to utilizing advanced spatially resolved plasma diagnostics in the tokamak divertor. These issues will become increasingly important once experiments commence on ITER.

Previous studies that address reflection effects in filtered imaging have used two main techniques. The first uses optical ray-tracing methods combined with a simplified first wall model that is often an axisymmetric surface.[5–7] The reflection properties of the wall in these models are often approximated as linear combinations of ideal specular and diffuse reflections. Whilst this is a good first order approximation, the reflecting properties of real physical materials have a wavelength dependence and roughening effects that depart from this idealized model.[8,9] In addition, the reflecting features observed in filtered camera images are always nonaxisymmetric.[5] This is likely due to the fact that the as-manufactured tokamak first walls are made from discrete tiles and exhibit complicated 3D structures that break axisymmetry. Both of these observations motivate the need to include a realistic 3D wall geometry model and a more physically accurate reflection model in optical ray-tracing approaches.

The most advanced previous ray-tracing study that attempted to include non-axisymmetric wall features was undertaken at the COMPASS tokamak.[6] An image of the vessel under diffuse background light captured all the asymmetric reflectivity patterns (e.g., diagnostic ports and limiters) and was used to mask a toroidally symmetric reflection model. This approach yielded significantly improved results over the normal axisymmetric model.[6] However, the challenge with this technique is to achieve a background light source that sufficiently resembles what would be present in a real tokamak experiment. In some machines, this may be difficult or even impossible.

The other main technique is to treat the reflected light as an undesired piece of information from the background, i.e., an offset of the primary data. In this type of analysis, an iterative algorithm might be used to converge to a self consistent "reflection corrected" image.[5] Otherwise, the reflected signal is modeled as a polluting noise source in a Bayesian framework such as MINERVA.[10,11] Both

of these techniques have shown promise but would not be as effective as a more realistic forward model where local geometry information and material properties can provide a powerful constraint on the reflection behavior. However, this does not preclude a possible hybrid ray-tracing Bayesian approach in future work.

Reflection effects are also a major issue with spectroscopic diagnostics on ITER where reflected light could contaminate spectral signals and jeopardize the usefulness of measurements.[12–18] Some of these studies utilized LightTools,[19] a commercially available ray-tracer, for simulating the magnitude of reflected light and to test possible mitigation strategies. These simulations were capable of using the full engineering models for the ITER first wall and more advanced reflection models.[15,16,18] They also demonstrated the ability to pre-compute reflection response matrices to obviate the need for on demand ray-tracing.[16] However, as a commercial ray-tracer, LightTools does not provide a suitable interface to tokamak plasma simulations. Instead the plasma emission was approximated by a set of cylinders of uniform emissivity derived from the source plasma simulation. Whilst being suitable for the diagnostic applications explored, such a reduced representation might not scale well to more general studies.

II. SCOPE OF THE WORK

In this work, we develop a state-of-the-art forward model for divertor filtered camera imaging using the CHERAB code.[20–22] CHERAB is a software framework developed with support from the EUROfusion JET[23] and Medium Sized Tokamak (MST)[24] science programs for modeling spectroscopic diagnostics with the Raysect ray-tracing package.[25] The CHERAB code was configured to model scrape-off layer line emission from plasma fluid simulations in SOLPS[26] and EDGE2D-EIRENE.[27] Realistic wall reflections are included by incorporating the 3D engineering geometry and physically motivated reflection models with fitted coefficients. Finally, high fidelity camera inversions including reflection effects are demonstrated by generating a set of sensitivity matrices, negating the need for on demand ray-tracing. The degree of uncertainty introduced by neglecting reflections in standard inversion techniques is quantified.

III. LIGHTING EQUATIONS AND MATERIAL MODELS

The total power (radiant flux) arriving on a surface is given by the integral of the incident emission over the collecting solid angle Ω and surface area A

$$\Phi = \int_A \int_\Omega \int L_i(\mathbf{x}, \omega, \lambda) \times \cos(\theta) d\lambda d\omega dA. \tag{1}$$

Here, $L_i(\mathbf{x}, \omega, \lambda)$ is the incident radiance arriving at a given point $\mathbf{x}$ and incident compound angle ω on the observing surface. The $\cos(\theta) = |\tilde{\omega} \cdot \vec{n}|$ term is a geometry factor describing the increase in an effective observing area as the incident rays become increasingly parallel to the surface.

The combination of the observing point $\mathbf{x}$ and incident compound angle ω defines a geometrical path known as a ray in the ray-tracing literature. In this work, we follow the literature conventions by considering the ray paths in the reverse direction, i.e., the ray's origin is actually the physical terminating point and the ray's

terminating surface, the point where the ray first intersects with an object surface, would be the physical origin of that optical ray path. Geometric optics are reversible, and the reverse formulation is computationally more efficient when the observer is small with respect to the emitter.[8]

The amount of incident radiance that arrives along a given ray path is given by the sum of the outgoing emission on the ray's terminating surface and the integral of all volumetric emission over the intermediate distance. If we label the path origin at the observer as $\mathbf{x}_1$ and first surface intersection point as $\mathbf{x}_2$, the equation for incident radiance can be expressed as

$$L_i(\mathbf{x_1}, \omega_i, \lambda) = L_o(\mathbf{x_2}, \omega_o, \lambda) + \int_{\mathbf{x_1}}^{\mathbf{x_2}} \frac{L_e(\mathbf{x}, \omega_r, \lambda)}{d\mathbf{x}} d\mathbf{x}. \quad (2)$$

The subscripts i and o are used on variables to denote the incoming and outgoing vector quantities, respectively. $L_e(\mathbf{x}, \omega_r, \lambda)$ is the local emission function from a given point of space due to volumetric emission. In the case of anisotropic volumetric emission, ω_r provides the ray angle in global coordinates. $L_o(\mathbf{x_2}, \omega_o, \lambda)$ is the outgoing radiance from the ray's terminating surface (Fig. 1).

These equations can be extended to form the fundamental lighting equations by considering how incident light is redistributed spectrally at a given surface through its material response function.[8,28] The amount of light that leaves a surface along a given outgoing angle, ω_o, at point $\mathbf{x}$ on an object is given by the sum of the light emitted at the object's surface and the total light reflected from all other sources

$$L_o(\mathbf{x}, \omega_o, \lambda) = L_e(\mathbf{x}, \omega_o, \lambda) + L_r(\mathbf{x}, \omega_o, \lambda). \quad (3)$$

$L_e(\mathbf{x}, \omega_o, \lambda)$ and $L_r(\mathbf{x}, \omega_o, \lambda)$ are the local contributions from surface emission and reflection, respectively, at surface point $\mathbf{x}$ along angle ω_o. The reflected light contribution can be in turn calculated by the integral over all incoming spectral radiance weighted by the surface response function

$$L_r(\mathbf{x}, \omega_o, \lambda) = \int_\Omega L_i(\mathbf{x}, \omega_i, \lambda) \times f_r(\omega_i, \omega_o, \lambda) \times \cos(\theta_i) d\omega_i. \quad (4)$$

This equation is similar to Eq. (1) with the addition of the bidirectional reflectance distribution function (BRDF) term $f_r(\omega_i, \omega_o, \lambda)$.[8,9,28] The BRDF is a weighting function that describes
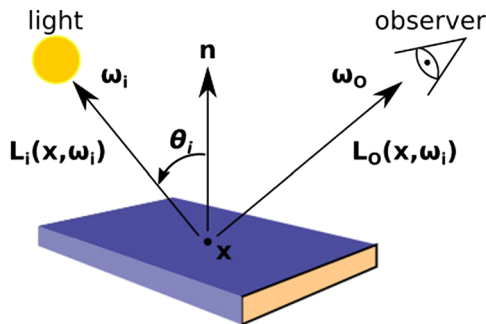

FIG. 1. Outgoing light emission from a surface is described in terms of the sum of the local surface emission and the integral of all incoming emission redistributed into the observation path, geometry for Eqs. (3) and (4).

the redistribution of incident light into outgoing reflections, L_r, and transmission/absorption inside the material.

The two ideal limits of f_r are specular (f_s) and diffuse/Lambertian (f_d) behavior. Ideal specular reflection behaves like a mirror surface where the incoming light is perfectly reflected into one specular angle, ω_s. This specular angle can be defined with respect to the incoming light angle and surface normal $\hat{n}$ as

$$\omega_s = 2(\omega_i \cdot \hat{n})\hat{n} - \omega_i. \quad (5)$$

In the limit of perfect mirror like behavior, specular reflection behaves like a vector delta function

$$f_s(\omega_i, \omega_o) = \rho_s(\omega_i)\delta(\omega_o - \omega_s). \quad (6)$$

Here, $\rho_s(\omega_i)$ is the specular reflection coefficient.

At the other limit, an ideal diffuse surface (matte paper, for example) will evenly redistribute incident light across all directions and hence has no angular dependence, $f_d(\omega_i, \omega_o) = \rho_d/\pi$, with ρ_d being the diffuse reflection coefficient.

A common approximation used in many of the previous studies is to model the BRDF function as a linear combination of the two ideal limits[5–7,15,18]

$$f_r(\omega_i, \omega_o, \lambda) = \rho_s\delta(\omega_i, \omega_o) + \rho_d/\pi. \quad (7)$$

To ensure conservation of energy, $\rho_s + \rho_d \leq 1$. The specular and diffuse coefficients, ρ_s and ρ_d, are often fitted to measured data or justified from reference material studies in the literature.

Real physical materials exhibit a complex combination of both specular and diffuse behaviors in addition to transmission and absorption. For this work, the BRDFs of fusion relevant materials were modeled with the Cook-Torrance BRDF,[9,29] which was parameterized in terms of the Fresnel equations and the GGX micro-facet surface model[30]

$$f_r(\omega_i, \omega_o, \lambda) = \frac{F(n, k)}{4} * \frac{D(\omega_i, \omega_o)G(\omega_i, \omega_o)}{\cos(\omega_i)\cos(\omega_o)}. \quad (8)$$

A similar model was used by Banerjee et al. with a simplified wall model for modeling spectral diagnostic reflections in Textor and ITER.[12] The Fresnel term, $F(n, k)$, is the analytic solution to Maxwell's equations for reflections from a smooth surface.[29–31] There are two sets of Fresnel equations, one for dielectric materials and the other for conductors. For each of these cases, there are two solutions depending on the polarization of the incident light. The Raysect ray-tracer currently does not support polarization, so here we have used the common approximation that light is unpolarized, i.e., randomly oriented with respect to the incoming ray direction. Under this assumption, the Fresnel reflectance is given by the average of the squares of the parallel and perpendicularly polarized light.[8] For the real and imaginary refractive index terms, n and k, we used measured data for relevant fusion materials published in the open literature, as shown in Fig. 2.

The rest of the right-hand side in Eq. (8) is a purely geometrical term. $D(\omega_i, \omega_o)$ is the GGX distribution,[30] a micro-facet distribution function that gives a statistical approximation to the distribution of micro-facets at the surface. The micro-facets reflect specularly, and hence, the bulk surface behavior is approximated as a statistical distribution of many small mirror-like surfaces. See Fig. 3 for a graphical representation of the micro-facet model.
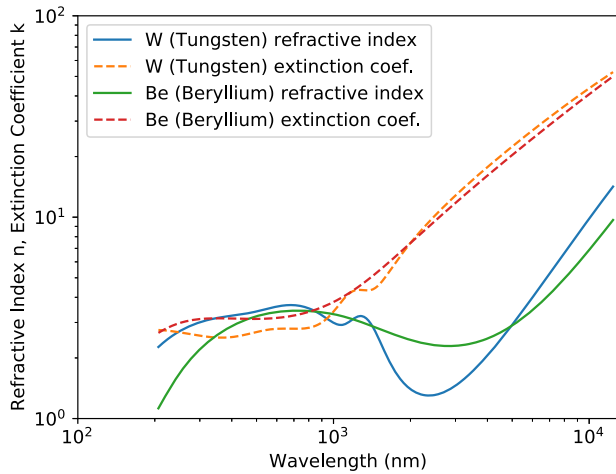
FIG. 2. Refractive index n and extinction coefficient k data for the main ITER-relevant first wall materials, Tungsten and Beryllium.[33,34]
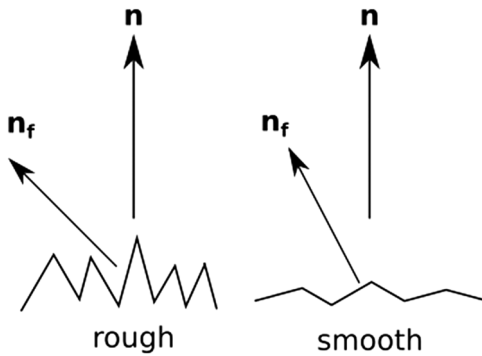

FIG. 3. A graphical representation of a micro-facet redistribution model which includes self-shadowing, internal reflections, and absorption. As the surface becomes rougher, there is a bigger spread in the distribution of facet normals $\mathbf{n_f}$ with respect to the surface normal $\mathbf{n}$.

$G(\omega_i, \omega_o)$ is a geometric attenuation factor that expresses the ratio of light that is occluded due to self masking and shadowing of microfacets.[9] Both $D(\omega_i, \omega_o)$ and $G(\omega_i, \omega_o)$ share a roughness parameter, $r \in [0, 1]$. Increasing r corresponds to an increase in the distribution of facet normals. In the limit of $r = 0$, Eq. (8) goes to the specular Fresnel equation result for a perfectly smooth surface. As $r \to 1$, Eq. (8) models a maximally rough surface, which tends toward an ideal Lambertian.

IV. MONTE-CARLO INTEGRATION

The lighting equation presented in Eq. (3) is exact but very difficult to evaluate analytically. The standard practice is to evaluate these functions with Monte Carlo importance sampling, which approximates the integral with a weighted average.[8,32] The Monte Carlo integral estimator for a given function f is given by the weighted sum

$$I \approx \frac{1}{N} \sum_{j=1}^{N} \frac{f(x_j)}{p(x_j)}. \tag{9}$$

Here, the function $f(x)$ is evaluated at N sample points x_j. These sample points are drawn from a probability density function

$$p(x_j) = \frac{q(x_j)}{\int q(x)dx}, \tag{10}$$

where $q(x)$ is the weight function for cases with non-uniform sample distributions.

The most natural way to discretize the lighting equation is in terms of N_r sample rays, constructed from 2D sample points $\mathbf{x_j}$ on the pixel area A_d and sample vectors ω_j on the unit hemisphere Ω. Under this scheme, the power collected on a given pixel surface area, as expressed in Eq. (1), would take the Monte Carlo form

$$\Phi \approx \frac{1}{N_r} \sum_{j=1}^{N_r} \frac{L_i(\mathbf{x_j}, \omega_j) \cos(\theta_j)}{p_A(\mathbf{x_j}) p_\Omega(\omega_j)}. \tag{11}$$

Here, $p_A(\mathbf{x_j})$ and $p_\Omega(\omega_j)$ are the probability density functions for the 2D sample points and ray vectors, respectively. For every ray launched that reaches a material surface, a second calculation is needed to evaluate the reflected light from that surface. Using the Monte Carlo ray-tracing integration scheme, the reflected spectral radiance from a surface at point $\mathbf{x}$ [Eq. (4)] can be expressed as

$$L_r(\mathbf{x}, \omega_o) \approx \frac{1}{N_r \Omega_{frac}} \sum_{j=1}^{N_r} \frac{L_i(\mathbf{x}, \omega_j) \times f_r(\omega_j, \omega_o) \times \cos(\theta_j)}{p_\Omega(\omega_j)}. \tag{12}$$

Note that the wavelength dependence λ of L_r, L_i, and f_r has been dropped in Eqs. (11) and (12) for brevity. The sum here is over N_r new rays launched from the ray-surface intersection point.

Although it is possible to evaluate Eqs. (11) and (12) directly, this is rarely done in practice because of the computational intensity of the problem.[8] Because the strike point radiators can be a few orders of magnitude brighter than the bulk plasma, this means that contributions from rays undergoing multiple reflections can be significant. Using a naive implementation with N_r rays per surface evaluation [Eq. (12)] leads to exponential growth in the number of rays required, becoming an intractable calculation method. To circumvent these problems and make the computations tractable, two further techniques are required, path-tracing and multiple importance sampling.[8]

Instead, path-tracing estimates the incoming radiance on ray i at the observer, $L_i(\mathbf{x_j}, \omega_j)$, as the sum of path contributions along a sampled path. Starting from the first intersection of the ith camera ray with the scene, we incrementally sample new path segments. The last path segment in the chain is determined by either intersecting a light source or by reaching a Russian roulette termination criterion. The paths are, therefore, generated in the physically reverse direction but evaluated in the forward direction.

In the case of Russian roulette path termination, at each new path segment, we evaluate whether the path has terminated based on a configurable termination probability. The Russian roulette technique allows us to sample paths that are computationally expensive but make a small contribution to the final result. The path termination probability is tuned based on the expected contributions from longer multiple reflection light paths in the scene being studied.

Let us say, for example, that ray i has a total of N_p path segments. The radiance from the path segment $x_k \rightarrow x_{k-1}$ is given by the sum of all previous path contributions, the emitted radiance at the path segment's origin point and the integral of all emission along the path segment

$$L_p(x_k \rightarrow x_{k-1}) = \left(L_p(x_{k+1} \rightarrow x_k) + L_e(x_k, \omega_k) \right.$$
$$\left. + \int \frac{dL_e(x_k \rightarrow x_{k+1})}{dl} dl \right) \frac{f(\omega_k, \omega_{k-1}) \cos \theta_{k-1}}{p_\Omega(\omega_{k-1}) \Omega_{frac}}.$$

(13)

This formula can be evaluated in an iterative fashion from the ray source point all the way back to the observer. This technique achieves good numerical efficiency when paired with an appropriate path sampling technique, such as multiple importance sampling.[8,32] Importance sampling exploits the fact that the Monte-Carlo estimator converges faster when samples are taken from a distribution $p(x)$ that is similar to the function $f(x)$ in the integrand, i.e., the sample points have a higher density in the regions where the integrand is the largest. A graphical representation of the path tracing algorithm is shown in Fig. 4.

Some suitable candidate distributions include the cosine distribution, lighting distribution and material BRDF distribution.[8] The cosine distribution is advantageous because of the cosine weighting in the lighting equations. It is typically more efficient than a

FIG. 4. A graphical representation of the path-tracing algorithm. (a) Candidate ray paths are first traced in the reverse direction. At each material intersection, a new path segment is randomly selected using the multiple importance sampling technique. The overall path terminates when either the Russian roulette termination criteria is met or a bright surface light source is encountered. (b) The emission contributions along the path are integrated in the forward direction.

uniform hemisphere distribution since its distribution is weighted proportional to $\cos(\theta)$ and has a higher sample density at the top of the hemisphere. The lighting distribution generates vectors toward light sources in proportion to their emitting power. The material distribution draws samples proportional to the material response, as in Eq. (8).

It is difficult to construct a single sampling distribution that represents a physically relevant scene. Instead, the integrand of the lighting equations can be approximated as sums and products of the underlying features in a scene. For example, consider a scene consisting of two light sources $(f_{L1}(x), f_{L2}(x))$, a single reflecting material $(f_{BRDF}(x))$ and a detector with a known sampling function $(f_d(x))$. The lighting equation integrand could be approximated as

$$f(x) = (f_{L1}(x) + f_{L2}(x)) * f_{BRDF}(x) * f_d(x).$$

(14)

Ideally we would sample all candidate distributions in a physical scene. Multiple importance sampling is a generalization of the importance sampling equation [Eq. (9)] which allows us to evaluate the lighting equations by simultaneously sampling multiple important distributions.[32] When using multiple importance sampling, the estimator becomes

$$I \approx \sum_{j=1}^{N_j} \sum_{l=1}^{n_l} \frac{w_j(x_{j,l}) f(x_{j,l})}{n_l p(x_{j,l})}.$$

(15)

Here, the index pair j, l is used to indicate the lth sample from the jth distribution. In the example case above, we had four relevant distributions $(N_j = 4)$ each with their associated sampling strategies $[f_{L1}(x), f_{L2}(x)), f_{BRDF}(x), \text{and } f_d(x)]$. Essentially we would draw n_l samples from each of the important distributions and evaluate the standard importance sampling equation [Eq. (9)]. The samples from the different distributions were combined through the balancing heuristic weight function[32]

$$w_j(x) = \frac{N_j p_j(x)}{\sum_l n_l p_l(x)}.$$

(16)

Parameters for the individual distributions can be individually adjusted during ray-tracing based on the materials and lighting distributions encountered along a ray's path and the observation geometry. In this work, we used the plasma emission source locations and metal tile BRDFs as the importance sampling distributions.

V. JET CALIBRATION PHOTOS

In order to implement these techniques for real tokamaks, we need a good estimate of the BRDF function, $f_r(\omega_i, \omega_o)$, for the materials used. Ideally, one would have tabulated gonioreflectometer measurements for each type of first wall tile. In the absence of such suitable measurements, we developed a method for estimating the first wall BRDF function from a series of photographs of point light sources. These techniques are demonstrated on JET as a case study but the method is generally applicable to other machines.

Tokamak first walls are often constructed from a mix of different materials since different parts of the wall will have differing needs in terms of their exhaust power handling capability and
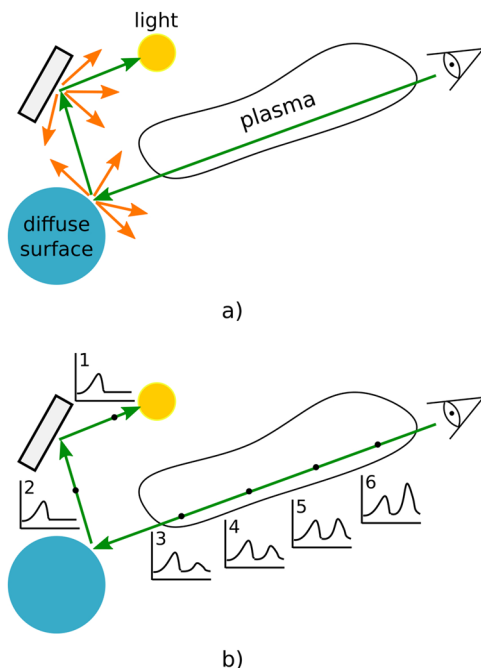
accessibility. Graphite tiles are a common choice for the first wall material in fusion experiments because of their relatively low cost, weight, and resilience under high exhaust power loads. However, as we move into the ITER era, many machines are moving to metal walls to be tritium compatible and to enable experiments in ITER-relevant plasma regimes,[35] e.g., JET-ILW, AUG, EAST, and WEST.

Figure 5 shows a rendering of the JET ITER-like wall with protective tiles color coded by their material composition. Bulk tungsten tiles are only used for a limited range of divertor tiles where the exhaust power loading demands are highest. Tungsten coated Carbon Fiber Composite (CFC) tiles are used for the rest of the divertor tiles, whilst pure beryllium or beryllium coated CFC are used for the majority of the limiter tiles.

It is possible to estimate the BRDF from a series of photos of a point light source providing the light positions and camera configuration are accurately known. Consider, for example, the in-vessel photograph of a point light source in Fig. 6(a). Each pixel in the image corresponds to a single incoming and outgoing vector combination in the BRDF coordinate space at the intersection point. If contributions from multiple reflection paths can be neglected to the first order, then the variation in the relative intensities of each pixel will correspond to the proportional BRDF changes in the material's BRDF space. Because of the toroidal (or cylindrical) shape of tokamak first walls, the pixels in a single image can span a large amount of the BRDF parameter space. And, hence, through changing the point light position across a number of images, the set of photos can provide a powerful fitting constraint on a given material's BRDF function *in lieu* of direct measurements.

At JET, there are eight in-vessel lights spaced equally around the top of the machine. A Nikon D3X SLR camera was mounted on the in-vessel robotic manipulator to provide a wide field of view. The camera position and distortion matrix were fitted with the Calcam camera calibration code.[36] All other light sources were turned off, while each in-vessel light was illuminated in turn providing a set of eight photographs. A single example photograph from the set is shown in Fig. 6(a).

FIG. 6. Measured (a) and simulated (b) JET IVIS light images for calibration and benchmarking of material BRDF properties. The regions of interest marked in orange (a) are identified for later discussion.
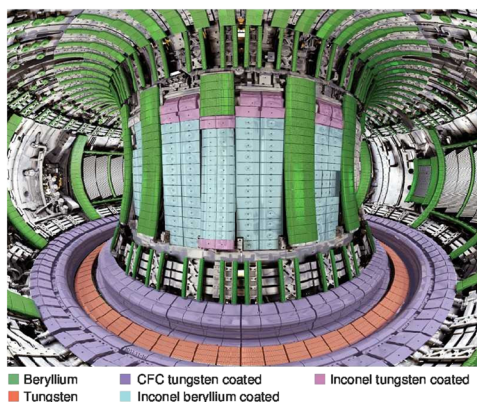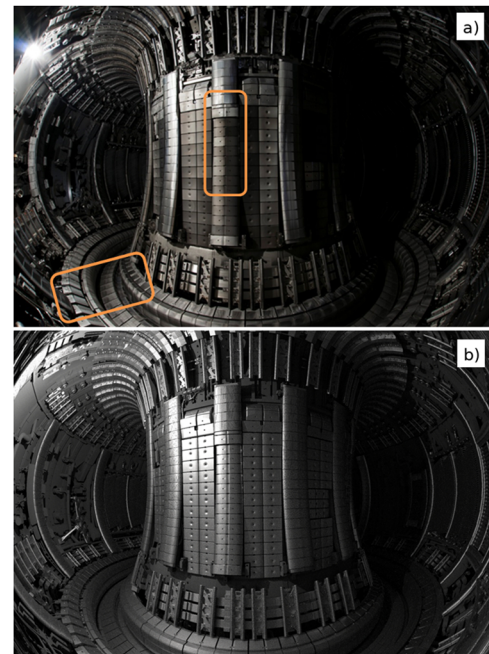

FIG. 5. Rendered image of the JET ITER-like wall CAD model with the first wall tiles color coded by their material composition. Figure provided courtesy of EUROfusion (© EUROfusion).

The pixels in each photograph were ray-traced to determine their intersection point in the vessel. Any intersection with no clear sight-line to the light source was eliminated. The remaining pixels were grouped by their intersecting material and mapped to a point in the material's BRDF parameter space. At any given wavelength, the BRDF function $f_r(\omega_i, \omega_o)$ is parameterized in terms of the incoming and outgoing ray vectors, ω_i and ω_o, respectively. If $f_r(\omega_i, \omega_o)$ is isotropic, these two vectors can be described by two polar angles, θ_i and θ_o, and the azimuthal angle ϕ between ω_i and ω_o. Hence, each remaining pixel can be mapped to a point in $(\theta_i, \theta_o, \phi)$.

Figure 7 illustrates an example of the BRDF parameter space coverage from the six point light locations that were used. Two of the light positions were not used in the analysis because they were on the occluded side of the machine and hence had poor direct coupling to the camera pixels.

For each measured image, a set of simulated images were ray-traced with Raysect using the refractive index data shown in Fig. 2 and a variable roughness parameter from Eq. (8). The roughness parameter was scanned over the range $0 < r < 0.5$ in each set of simulated images. For each individual roughness value, the mean squared error between the measured images and simulated images was calculated for each material. A polynomial was fitted to the resulting χ^2 surface for each material, with the minimum determining the best fit roughness parameter. An example fit to the JET beryllium limiter tiles is given in Fig. 8, with the best fit values displayed in Table I.

Good quantitative agreement was achieved, as demonstrated by the comparison of a calibration image and the companion simulation image in Fig. 6(b). The regions of greatest disagreement in
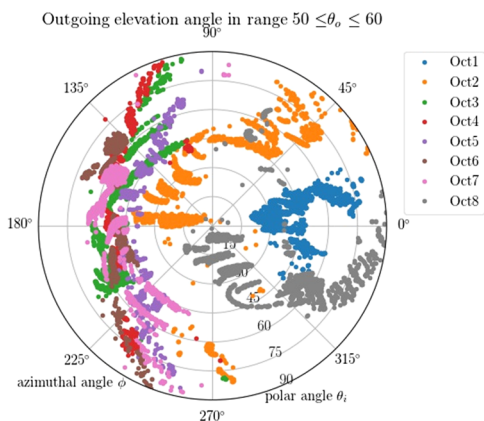
FIG. 7. A plot of the individual pixels from the measured images re-mapped into the tungsten tile material BRDF coordinate space $(\omega_i, \omega_o) \rightarrow (\theta_i, \theta_o, \phi)$. Any pixels that did not correspond to an intersection with a tungsten tile were discarded. The pixels are color coded by their source photograph, indicating the JET octant in which the point light source was located.
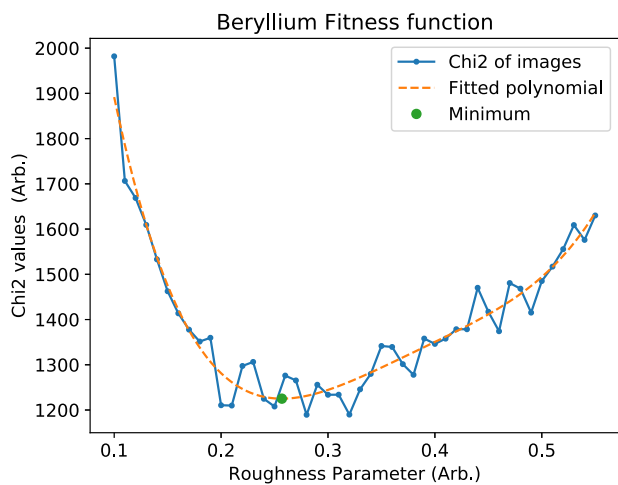

FIG. 8. An example of the fitted roughness parameter for the JET beryllium limiters. At each roughness value, the mean squared error between the measured and simulated images was computed.

Fig. 6 tend to be in the vicinity of the coated tile groups. These materials have an anisotropic BRDF response function that could not be captured in the material model used and were approximated as Lambertian.

TABLE I. Fitted roughness parameters for the beryllium and tungsten tiles in the JET ITER-like wall.

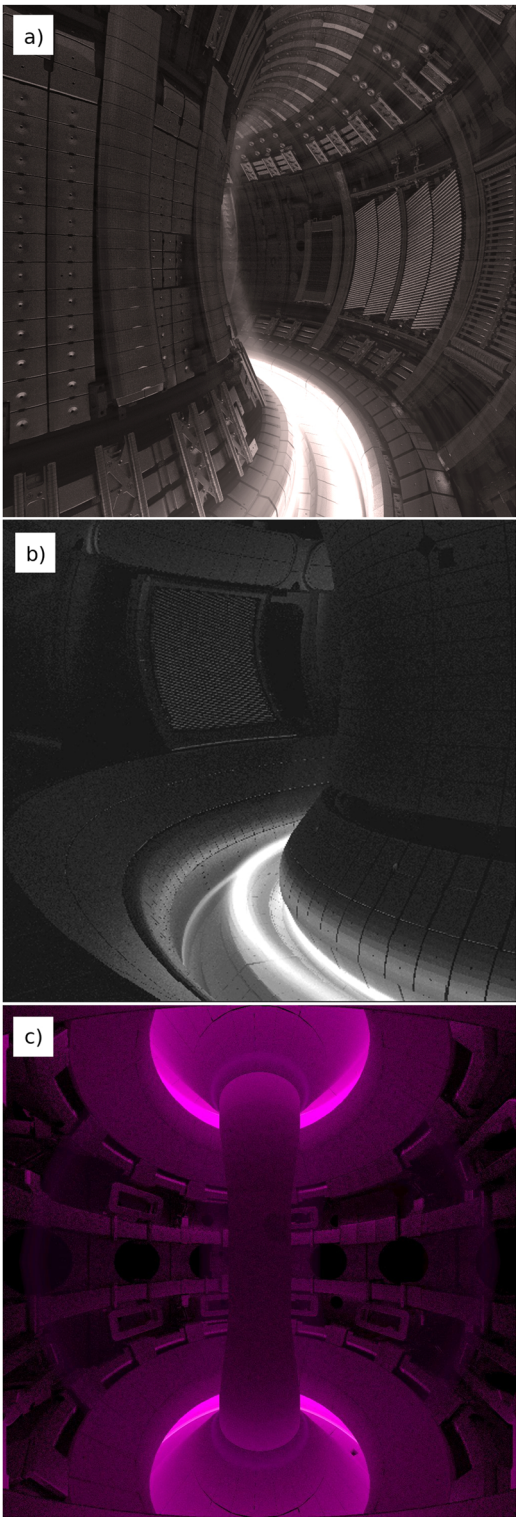| Material	Roughness parameter r
Beryllium limiters	0.257
Tungsten divertor	0.291

FIG. 9. Simulated images of (a) D_α emission from JET (black and white), (b) D_α emission from AUG, and (c) predicted visible emission from the Balmer series in MAST-U as would be measured by the mid-plane camera.
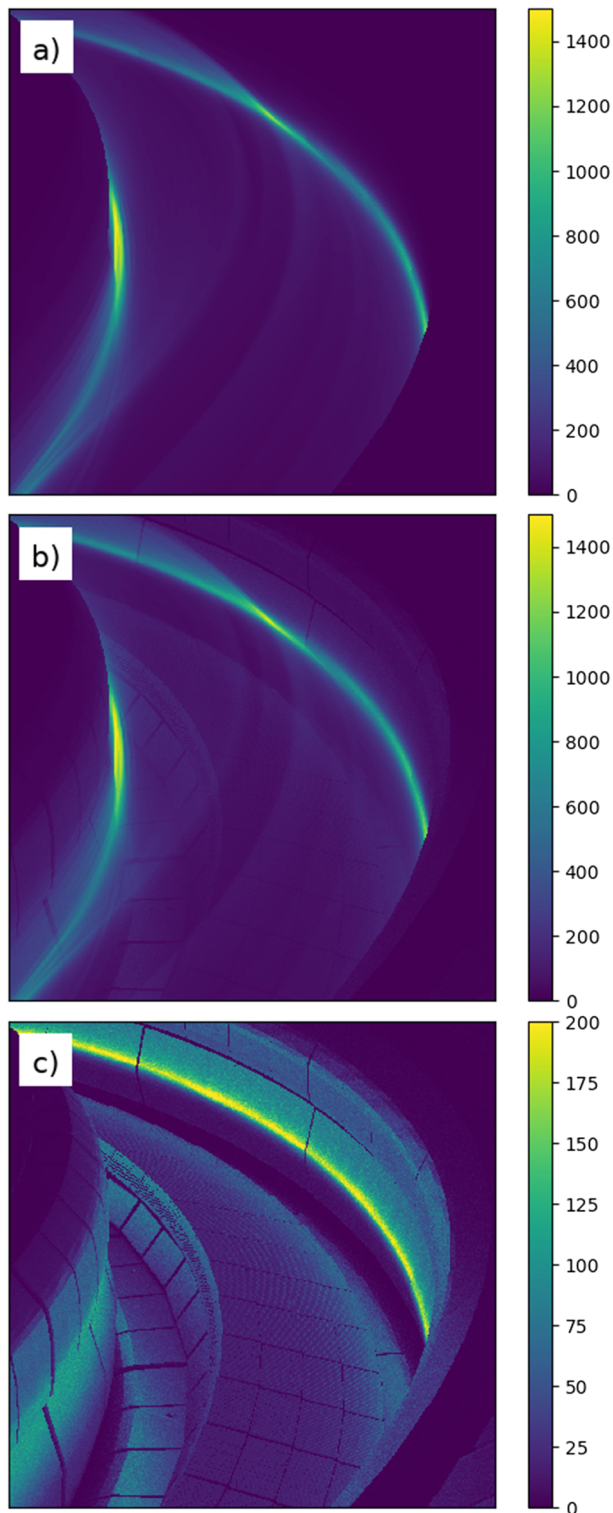
FIG. 10. (a) Forward modeled plasma emission for the KL11 JET camera, (b) same emission scenario with reflection effects added, and (c) the subtraction of images (a) and (b), giving the isolated contribution from reflected light.

VI. FORWARD MODELING FILTERED CAMERAS

Having quantitatively fitted the JET first-wall material reflection properties, it is thereby possible to generate synthetic photo-realistic images of the interior of fusion devices. The utility of such synthetic images lies in our ability to study the diagnostic capabilities of filtered visible cameras, assessing their ability to make certain measurements, predicting their diagnostic capabilities on future devices and performing direct comparisons of simulations with measured camera images.

The emission of a visible spectral line, $\epsilon_{i \to j}$, at the plasma edge is given by the population number density of ions in the upper state multiplied by the spontaneous emission coefficient for the transition.[37] The emissivity coefficients can be obtained by relating the emission to the excitation processes through a collisional-radiative model. The three dominant processes that can lead to an ion being in an excited state are excitation of the ion through electron impact, free electron recombination onto the parent ion and recombination through charge exchange.[37] Therefore, for a given plasma ion with charge z, the intensity of the line emission can be expressed as

$$\epsilon_{i \to j} = n_e n_i^{z+} \sigma_{i \to j}^{(exc)} + n_i^{(z+1)+} \left(n_e \sigma_{i \to j}^{(rec)} + n_d \sigma_{i \to j}^{(cx)} \right), \qquad (17)$$

where $\sigma_{i \to j}^{(exc)}$, $\sigma_{i \to j}^{(rec)}$, and $\sigma_{i \to j}^{(cx)}$ are the respective photon emissivity coefficients for the dominant population processes. The electron density is n_e, with the emitting ion density of a specified charge state given by n_i and charge exchange donor species density n_d.

For the simulations, the relevant plasma population densities and temperatures at the plasma edge are from SOLPS[26] or EDGE2D-EIRENE[27] plasma fluid simulations. The photon emissivity coefficients were taken from the Open-ADAS web repository.[38]

Figures 9(a) and 9(b) shows forward modeled synthetic images of D_α light for JET and AUG. Such images can be used to assess the physical accuracy of the underlying plasma simulations when compared quantitatively with real measurements. Figure 9(c) shows a predicted observation of a detached plasma in MAST-U. For this simulation, the light is given by the sum over the first five terms of the deuterium Balmer series. In the MAST-U image, the edge emission of the plasma at the mid-plane is predicted to be much less pronounced than in MAST due to the increased compression ratio of neutrals between the midplane and divertor during detached operation.

In Fig. 10, we quantify the impact of reflections on measurements made using the JET's KL11 filtered divertor camera. An EDGE2D-EIRENE simulation was used to calculate the raw plasma emission in Fig. 10(a). Reflection effects are added to the image in Fig. 10(b), with the image subtraction giving the reflection only contribution in Fig. 10(c). The reflected light is an order of magnitude weaker than the brightest emission features at the strike points; however, it is clear from Fig. 10(b) that the reflected light can dominate the image for pixels that do not see the brightest emission regions.

VII. INVERSIONS WITH REFLECTIONS

Routine inversion of these images using a direct ray-tracing forward model would be infeasible due to the immense computational resources required for reflection ray-tracing. However, the
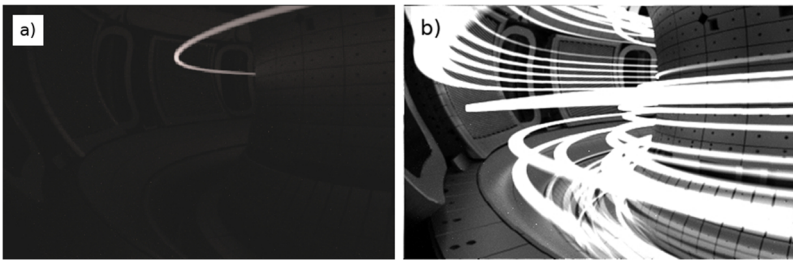
FIG. 11. (a) A slice of the sensitivity matrix representing a single voxel basis function for the AUG midplane filtered camera. (b) A synthetic image produced by the matrix multiplication of a random set of basis functions.

camera viewing geometry and optical properties are generally constant for the duration of an experimental campaign. Let us also make the assumption that the first wall conditions do not change significantly between shots. This would mean that only the distribution and intensity of emitters changes during the shot. The wall reflection properties and the camera response to individual geometric sources are constant, allowing these response functions to be precomputed.

The ray-tracing techniques described in this work were used to generate a set of sensitivity matrices that describe the coupling
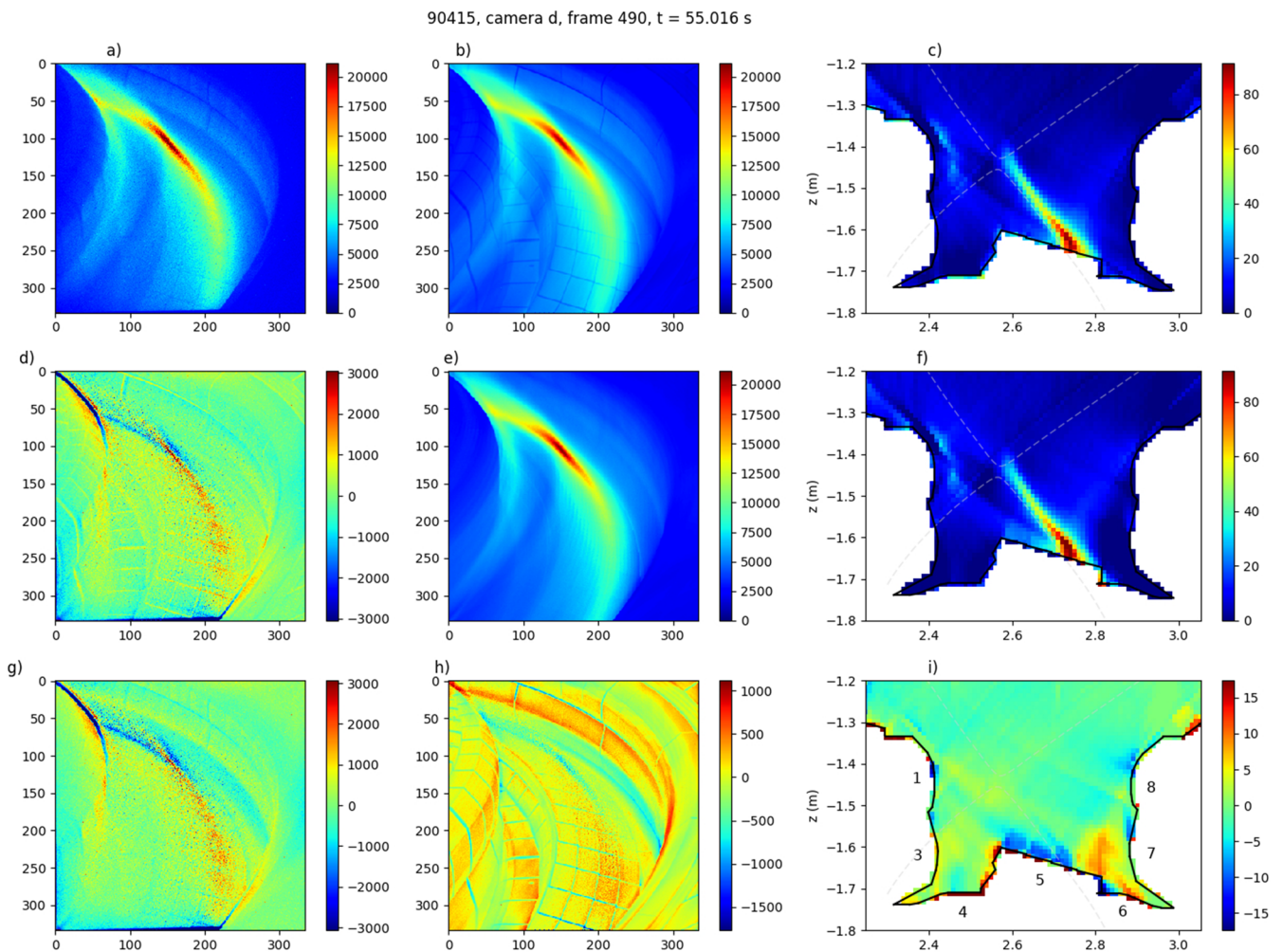

FIG. 12. (a) A measured image of D_α light from the JET KL11 D divertor camera, pulse #90415 at 55.016 s. The image was inverted using sensitivity matrices both with and without reflection effects. The inverted synthetic images [(b) and (e)] and accompanying emissivity profiles [(c) and (f)] are given for both cases. The differences between the measured and synthetic images are given in (d) [(a) - (b)] and (g) [(a) - (e)]. (h) Shows the level of reflected light added by the reflection model to the synthetic image [(b)-(e)] and (i) shows the resulting effect on the emissivity profiles [(c) - (f)]. The voxel grid used in this inversion extends into the main chamber.

of individual emitting plasma sources to the camera through the observer equations. The plasma emission sources were discretized into 3d voxels composed of a toroidally symmetric annulus with a uniform volume emissivity. The response of the camera to each voxel can be thought of as a set of basis functions into which a measured image can be linearly decomposed. Figure 11(a) shows an example of an individual voxel basis function. Figure 11(b) shows a synthetic image created by the matrix multiplication of a random set of voxel basis functions.

The resulting sensitivity matrix allowed camera inversions to be performed using established tomography techniques. There are a wide range of tomography algorithms in use across fusion diagnostics. For this work, we elected to use the Simultaneous Algebraic Reconstruction Technique (SART), as described in Ref. 22.

The voxel grid was configured to have a high density of voxels in the divertor (~1 cm width) and a coarser (~3 cm width) in the main chamber. It is common in filtered camera tomography to use a trimmed voxel domain where only direct emission is modeled, for example, by limiting the inversion grid to voxels only in the divertor. However, when modeling reflections, it is necessary to include emission sources that are outside the directly observed domain. Experiments with different voxel grid configurations demonstrated that extending the grid into the main chamber can significantly clean up the background halo artifacts and emission blobs at the edges of the domain.

In Fig. 12, we compare and contrast an example camera inversion with and without reflection effects included. The measured image in Fig. 12(a) is from a D_α filtered divertor camera at JET. The inverted synthetic images are shown in Figs. 12(b) and 12(e) with the underlying emissivity profiles in Figs. 12(c) and 12(f). Various difference images are also presented to aid the comparisons. The tile position labels are included in Fig. 12(i).

The main differences in the inverted divertor emission patterns when adding the reflections in Fig. 12 is the reduction in volume emission artifacts above tile 5 and tile 1. A lot of the bright isolated

voxels on the surfaces of these tiles disappear or are significantly reduced. The emission peak on tile 5 drops by 7% when reflections are taken into account. Overall, the emission intensity of the strike point radiator is over estimated when reflections are not taken into account. This in turn would lead to an error in the inferred plasma density when the inverted emission is used to infer physics parameters. The amount of error gets progressively worse as you move away from the bright radiators.

VIII. DISCUSSION

The ray-tracing techniques presented are expected to have the most impact on filtered camera imaging systems on metal wall machines. Polluting reflected light has long prevented the exploitation of these diagnostics. The improvement would be more modest, however, on carbon walled machines where the graphite produces much more diffuse reflecting features.

Although each individual ray-traced image can take several hours to compute, a typical inversion with the SART algorithm and the cached sensitivity matrix could be performed in a few minutes on a standard desktop PC. In the example case in Fig. 12, the inversion took 5 min using a single core of an Intel Xeon E5-2665 at 2.4 GHz. Further speed increases could be obtained in future through parallelization across multiple cores.

The calibration photos provided a good method for approximating the material BRDF properties of the bulk tungsten and beryllium tile groups. But as anticipated, there were a number of tile groups that showed a poor match between the calibration and simulation images. One such tile group is the inconel limiter tiles with a beryllium coating [highlighted in Fig. 5 with an example photo in Fig. 13(a)]. These tiles appeared to exhibit a highly anisotropic BRDF response function that could not be captured by the fundamentally isotropic material model that was used.

Another tile group that showed poor agreement was the tile 3 row of tungsten coated CFC tiles [highlighted in Fig. 5 with an
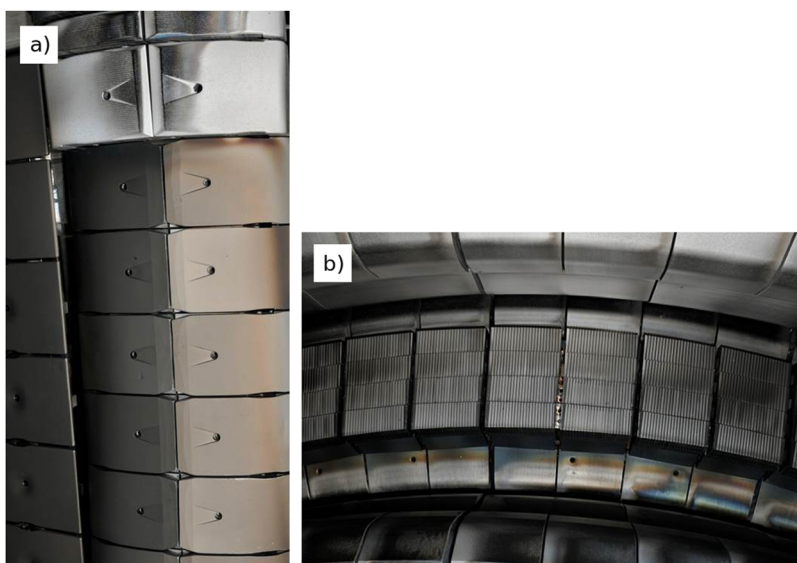

FIG. 13. Close up photographs of the regions of interest identified in Fig. 6. (a) A section of the inboard limiter with beryllium coated inconel tiles that have an anisotropic BRDF. (b) A section of the tungsten divertor with clear visible indications of plasma surface interactions on the inboard tiles (lower part of the image).

example photo in Fig. 13(b)]. These tiles show evidence of plasma surface interactions resulting in a localized rougher surface, perhaps through sputtering and deposition. They are also near commonly used divertor strike point positions, and their surface coating appears to exhibit a complex spatially repeating pattern.

In future work, the reflection models developed in this paper could, in principle, be extended to materials with anisotropic BRDFs although the amount of data required to capture these material properties would be dramatically higher. In such cases, the calibration photo method developed in this paper would be insufficient. The tile BRDF model for all tile groups could be improved by using tabulated BRDF data measured using a spectral gonioreflectometer. Future work could aim to exploit the published gonioreflectometer measurements on the ITER first wall tiles[39] or repeat the measurements for the JET tiles.

The assumption that the wall material properties are changing slowly throughout an experimental campaign is crucial to enabling the use of the cached ray-tracing sensitivity data. This is because calculating the sensitivity matrices on a shot-to-shot basis would be computationally infeasible. Therefore, for the method to be suitable, it is important that the material reflection properties are assessed throughout a campaign, perhaps through the in-vessel point light method developed in this paper. First wall material changes could be monitored over time by assessing the change to the BRDF fit in the calibration photographs. This may prove to be a valuable monitoring tool for machines where regular vessel access is restricted or expensive.

IX. CONCLUSIONS

A new technique for forward modeling filtered camera diagnostics has been developed that is capable of taking into account realistic reflection effects. This technique was implemented using the Raysect open source ray-tracer and the CHERAB spectroscopy framework.

It was shown that it is possible to measure and approximately fit the BRDF properties of most first wall tile components through a series of calibration photos of in-vessel point lights. This technique could be integrated into regular tokamak shutdown activities to verify the cached ray-tracing reflection model and as a method of monitoring the evolution of wall conditioning due to plasma-surface interactions.

Photo-realistic renderings of radiation scenarios for a number of fusion machines were demonstrated with an unprecedented level of detail. These high-fidelity forward models can be used to assess the scientific value of new and existing filtered camera plasma diagnostics.

To enable routine inversions of measured camera data, sensitivity matrices for a divertor voxel grid were calculated including the reflection effects. This allows inversions to be performed with matrix multiplication in minutes, a process that would be infeasible with on demand ray-tracing. These techniques may enable the wider exploitation of filtered scientific cameras in divertor science studies.

ACKNOWLEDGMENTS

This work has been carried out within the framework of the EUROfusion Consortium and has received funding from

REFERENCES

[1] I. H. Hutchinson, *Principles of Plasma Diagnostics* (Cambridge University Press, 2005).

[2] S. S. Henderson *et al.*, Nucl. Fusion **58**, 016047 (2017).

[3] J. R. Harrison, S. W. Lisgo, K. J. Gibson, P. Tamain, J. Dowling, and MAST Team, J. Nucl. Mater. **415**, S379 (2011).

[4] A. Huber *et al.*, J. Nucl. Mater. **438**, S139 (2013).

[5] J. Harhausen, "Interpretation of Dα imaging diagnostics data on the ASDEX upgrade tokamak," Ph.D. thesis, Ludwig-Maximilians-Universität München, 2009.

[6] M. Odstrčil, J. Mlynář, V. Weinzettl, P. Háček, T. Odstrčil, G. Verdoolaege, M. Berta, T. Szabolics, and A. Bencze, Rev. Sci. Instrum. **85**, 013509 (2014).

[7] K.-D. Zastrow, S. R. Keatings, L. Marot, M. G. O'Mullane, G. De Temmerman, and Jet-EFDA Contributors, Rev. Sci. Instrum. **79**, 10F701 (2008).

[8] M. Pharr and G. Humphreys, *Physically Based Rendering: From Theory to Implementation* (Morgan Kaufmann, 2016).

[9] R. Montes and C. Ureña, "An overview of BRDF models," Technical Report LSI-2012-001, University of Grenada, 2012.

[10] J. Svensson, "Nonparametric tomography using Gaussian processes," JET Internal Report No. EFDA-JET-PR(11)24, 2011.

[11] J. Svensson and A. Werner, in *IEEE International Symposium on Intelligent Signal Processing-WISP* (IEEE, 2007), Vol. 955.

[12] S. Banerjee, P. Vasu, M. von Hellermann, and R. J. E. Jaspers, Plasma Phys. Controlled Fusion **52**, 125006 (2010).

[13] C. Guillemaut, R. A. Pitts, A. S. Kukushkin, and M. O'Mullane, Fusion Eng. Des. **86**, 2954 (2011).

[14] A. B. Kukushkin *et al.*, "Divertor stray light analysis in JET-ILW and implications for the H-α diagnostic in ITER," AIP Conf. Proc. **1612**, 97 (2014).

[15] S. Kajita, M. De Bock, M. Von Hellermann, A. Kukushkin, and R. Barnsley, Plasma Phys. Controlled Fusion **57**, 045009 (2015).

[16] S. Kajita, E. Veshchev, R. Barnsley, and M. Walsh, Contrib. Plasma Phys. **56**, 837 (2016).

[17] V. S. Neverov, A. B. Kukushkin, M. F. Stamp, A. G. Alekseev, S. Brezinsek, M. von Hellermann, and JET Contributors, Nucl. Fusion **57**, 016031 (2016).

[18] S. Kajita, E. Veshchev, M. De Bock, R. Barnsley, M. Von Hellermann, and M. Walsh, Fusion Sci. Technol. **74**, 37 (2018).

[19] See https://optics.synopsys.com/lighttools/ for LightTools webpage (current as of October 2, 2018).

[20] C. Giroud, A. Meakins, M. Carr, A. Baciero, and C. Bertrand (2018), "CHERAB spectroscopy modelling framework," Zenodo, version v0.1.0, http://doi.org/10.5281/zenodo.1206142.

[21] M. Carr *et al.*, "Towards integrated data analysis of divertor diagnostics with ray-tracing," in 44th European Physical Society Conference on Plasma Physics, Belfast, Northern Ireland UK, 26–30 June 2017, http://ocs.ciemat.es/EPS2017PAP.

[22] M. Carr *et al.*, Rev. Sci. Instrum. **89**, 083506 (2018).

[23] X. Litaudon *et al.*, Nucl. Fusion **57**, 102001 (2017).

[24] H. Meyer *et al.*, Nucl. Fusion **57**, 102014 (2017).

[25] A. Meakins and M. Carr (2017), "Raysect Python raytracing package," version v0.4.0, Zenodo, http://doi.org/10.5281/zenodo.1205064.

[26] S. Wiesen et al., J. Nucl. Mater. **463**, 480 (2015).

[27] R. Simonini, G. Corrigan, G. Radford, J. Spence, and A. Taroni, Contrib. Plasma Phys. **34**, 368 (1994).

[28] J. T. Kajiya, "The rendering equation," ACM SIGGRAPH Comput. Graphics **20**, 143 (1986).

[29] R. L. Cook and K. E. Torrance, "A reflectance model for computer graphics," ACM Trans. Graphics **1**, 7 (1982).

[30] B. Walter, S. R. Marschner, H. Li, and K. E. Torrance, "Microfacet models for refraction through rough surfaces," in *Proceedings of the 18th Eurographics Conference on Rendering Techniques* (Eurographics Association, 2007), p. 195.

[31] D. J. Griffiths, *Introduction to Electrodynamics*, 3rd ed. (Prentice-Hall, Upper Saddle River, New Jersey, 1999), pp. 301–306.

[32] E. Veach, "Robust Monte Carlo methods for lighting simulation," Ph.D. thesis, Stanford University, 1997.

[33] A. D. Rakić, A. B. Djurišić, J. M. Elazar, and M. L. Majewski, Appl. Opt. **37**, 5271 (1998).

[34] M. N. Polyanskiy, Refractive index database, https://refractiveindex.info; accessed on 21 September 2018.

[35] G. F. Matthews et al., Phys. Scr. **T145**, 014001 (2011).

[36] S. Silburn, J. Harrison, M. Smithies, A. Wynn, T. Farley, and J. Cavalier (2018), "Calcam," Zenodo, version 1.9.4, http://doi.org/10.5281/zenodo.1478555.

[37] H. J. Kunze, *Introduction to Plasma Spectroscopy* (Springer Science and Business Media, 2009), Vol. 56.

[38] H. P. Summers and M. G. O'Mullane, "Atomic data and modelling for fusion: The adas project," AIP Conf. Proc. **1344**, 179 (2011).

[39] M. B. Yaala et al., "Wall reflection measurements," in 31st Mtg. ITPA Topical Group Diagnostics, St. Paul Lez Durance, France, 7–10 November 2016.